Rock Mech Rock Eng (2017) 50:3157–3173
https://doi.org/10.1007/s00603-017-1280-5

ORIGINAL PAPER

Pore Pressure and Stress Distributions Around a Hydraulic Fracture in Heterogeneous Rock

Qian Gao[1] · **Ahmad Ghassemi**[1]

Received: 8 December 2015 / Accepted: 11 July 2017 / Published online: 8 August 2017

Abstract One of the most significant characteristics of unconventional petroleum bearing formations is their heterogeneity, which affects the stress distribution, hydraulic fracture propagation and also fluid flow. This study focuses on the stress and pore pressure redistributions during hydraulic stimulation in a heterogeneous poroelastic rock. Lognormal random distributions of Young's modulus and permeability are generated to simulate the heterogeneous distributions of material properties. A 3D fully coupled poroelastic model based on the finite element method is presented utilizing a displacement–pressure formulation. In order to verify the model, numerical results are compared with analytical solutions showing excellent agreements. The effects of heterogeneities on stress and pore pressure distributions around a penny-shaped fracture in poroelastic rock are then analyzed. Results indicate that the stress and pore pressure distributions are more complex in a heterogeneous reservoir than in a homogeneous one. The spatial extent of stress reorientation during hydraulic stimulations is a function of time and is continuously changing due to the diffusion of pore pressure in the heterogeneous system. In contrast to the stress distributions in homogeneous media, irregular distributions of stresses and pore pressure are observed. Due to the change of material properties, shear stresses and nonuniform deformations are generated. The induced shear stresses in heterogeneous rock cause the initial horizontal principal stresses to rotate out of horizontal planes.

✉ Ahmad Ghassemi
ahmad.ghassemi@ou.edu

[1] Mewbourne School of Petroleum and Geological Engineering, The University of Oklahoma, Norman, OK 73019, USA

Keywords Hydraulic fracturing · Heterogeneous porous media · Poroelasticity · Refac · Stress reversal · Stress shadow

1 Introduction

Hydraulic fracturing is an essential technology to achieve economic production in unconventional hydrocarbon reservoirs; these include tight gas sands, shale gas and coalbed methane. One of the most significant characteristics of shale source rock is the heterogeneity of reservoir properties, which affect the stress distribution, hydraulic fracture propagation and also fluid flow. However, to our knowledge the impact of heterogeneities on stress and pore pressure distribution around a hydraulic fracture has not been studied. In contrast, the induced stresses around pressurized fractures in an elastic or poroelastic homogeneous medium are well described in the literature (Kumar and Ghassemi 2015; Rawal and Ghassemi 2011; Sesetty and Ghassemi 2015; Warpinski and Branagan 1989).

Vandamme et al. (1989) and Ghassemi and Roegiers (1996) studied 2D and 3D poroelastic effects on hydraulic fracturing. Gordeyev (1993) derived analytical expression for the width of a 3D fracture in homogeneous poroelastic media. Zhou and Ghassemi (2011) used a fully coupled poroelastic displacement discontinuity (DD) method to study the response of a natural fracture in poroelastic media, while Ghassemi and Zhou (2011) investigated the impact of thermo-poroelastic effects on fracture width and injection pressure. The transient response of a uniformly pressurized fracture has been quantified by considering a pressurized Griffith crack in poroelastic and thermo-poroelastic media (Detournay and Cheng 1991; Ghassemi and Zhang 2006). Ge and Ghassemi (2008) calculated the

injection-induced stress using a thermo-poroelastic model. The potential failure regions around the pressurized fracture were evaluated.

Although extensive work, both theoretical and experimental, has been carried out on fluid flow in heterogeneous porous media (Durlofsky 1991; Guerillot et al. 1990; Warren and Price 1961), analysis of stress and pore pressure distributions in a heterogeneous poroelastic rock is rarely available. Hydraulic fracturing inevitably alters the stress distribution and fluid flow paths. Investigation of stress redistribution and fluid migration during hydraulic fracturing under heterogeneous reservoir conditions with natural fractures (Safari and Ghassemi 2015; Wang and Ghassemi 2012) will improve our understanding and will help technology development to optimize stimulation design.

The purpose of this study is to provide insight into the influence of heterogeneities in reservoir rock properties on the stress and pore pressure distributions during hydraulic fracturing. Sensitivity analyses are performed through variations of material properties which are used to characterize a poroelastic rock, e.g., Biot's effective stress coefficient, Young's modulus, drained and undrained Poisson's ratios. The drained and undrained material properties reflect two limiting behaviors of poroelastic rocks. The situation where the applied loads and deformations are slow relative to the time scale of fluid diffusion is called a drained response. The undrained response occurs when the fluid diffusion timescale is too short to allow alterations in the fluid mass content (Rice and Cleary 1976). The drained and undrained Poisson's ratios are evaluated under drained and undrained experimental conditions, respectively.

A 3D numerical model based on the finite element method (FEM) is developed and utilized. Numerical solutions are compared with analytical ones developed by Sneddon (1946) for a penny-shaped crack in an infinite, 3D elastic medium. The stress and pore pressure distributions are illustrated for both homogenous and heterogeneous scenarios. Also, zones of stress reorientation, i.e., areas where the principal stresses have rotated, are determined for both homogenous and heterogeneous cases, and zones of stress reversal (where the induced stresses change the principal stress magnitudes such that the minimum is now the maximum, i.e., a complete reversal) are shown.

2 Problem Description and Methodology

2.1 Problem Description

Usually, the information about subsurface rock properties is incomplete. One of the most important problems associated with reservoir characterization is that of determining the nature of heterogeneities that inevitably occur in formations. Theoretical and experimental investigations have provided reasonable descriptions of the physical processes that are involved in hydraulic fracturing. However, the uncertainty about the distributions of natural fractures, in situ stresses and formation properties, such as Young's modulus and permeability, leads to uncertainty in estimating or predicting the stress redistribution and the fluid flow during hydraulic fracturing. In this paper, we investigate the influence of heterogeneous distributions of Young's modulus and permeability on the reservoir rock during hydraulic fracturing. Intact rocks have higher Young's moduli than the rock masses consisting of the same intact materials but with discontinuities such as natural fractures. Also, the permeability of intact rocks is generally much smaller than that of rock masses. Young's modulus and permeability are both affected by the presence of discontinuities, and one could establish correlations between the two parameters; however, we consider them as independent.

A challenging aspect of dealing with reservoir heterogeneity is that it is possible to compute behaviors based on specific reservoir heterogeneity and physical models, but it is not possible to specify the in situ distribution of reservoir heterogeneity (Warren and Price 1961). A simple way to investigate the behavior of hydraulic fracturing in heterogeneous reservoirs is to perform stochastic (Monte Carlo) simulations (Fenton and Griffiths 2008). In this work, we first discuss the generation of random fields of Young's modulus and permeability. Then, the response of each geostatistical realization is simulated using a coupled fluid flow and geomechanical model. A realization of a random variable is the value generated from a stochastic simulation. Synthetic examples are studied to analyze the linkage between the degree of heterogeneity and the corresponding rock responses in terms of pore pressure and stress distributions.

2.2 Generation of Random Fields

The normal (or Gaussian) distribution is a widely used continuous probability distribution. Its probability density function can be characterized by a mean value μ and a variance σ^2. When the normal distribution is utilized to represent material properties, negative values may be generated (Fenton and Griffiths 2008), which do not have physical meaning. A simple way, commonly adopted in practice, is to use the lognormal distribution.

In our current study, only the Young's modulus and permeability are considered to be spatially random properties and are assumed to follow a lognormal distribution. An exponential semivariogram function $\gamma(L)$ is used to

specify the spatial correlation in observations measured at sample locations (Deutsch and Journel 1992),

$$\gamma(L) = C_0\left[1 - \exp\left(\frac{-3L}{a}\right)\right] \tag{1}$$

where L = lag distance, a = effective range of the variogram, and C_0 = sill value. Also, several methods for generating a Gaussian random field, which is completely characterized by the mean and covariance values, can be found in Fenton and Griffiths (2008). To simplify the problem, the heterogeneous fields are assumed to be isotropic, that is, the correlation structure in both the horizontal and vertical directions is assumed to be the same. The assumption of isotropy admittedly has its limitations. Reservoirs often exhibit anisotropic characteristics, but in this study we focus on heterogeneous distributions of material properties. The role of anisotropy in stimulation has been considered by Sesetty and Ghassemi (2016).

The unconditional Gaussian random field is commonly referred to as spatially correlated random field. A random field that preserves certain known data at specific points is called a conditional random field (Fenton and Griffiths 2008). For unconditional simulations, the mean values of Young's modulus and permeability are constant. The standard deviations are varied to evaluate the effects of input variability on the physical responses of a reservoir. The parameters of the transformed log normal Gaussian random filed are obtained from the following equation (Fenton and Griffiths 2008):

$$\sigma_{\ln}^2 = \ln\left(1 + \left(\frac{\sigma}{\mu}\right)^2\right) \tag{2}$$

$$\mu_{\ln} = \ln(\mu) - \frac{1}{2}\sigma^2 \tag{3}$$

where σ and μ are variance and mean of the normal distribution, $\sigma_{\ln}$ and $\mu_{\ln}$ are variance and mean for the log-normal distribution.

The actual values are transformed by scaling with respect to the unit-variance Gaussian random field $G(x)$ according to

$$f(x) = \exp(\mu_{\ln} + \sigma_{\ln} G_i) \tag{4}$$

where G_i is the value at the ith element of a zero mean, unit-variance Gaussian random field $G(x)$.

2.3 Poroelastic Model

The coupled deformation/diffusion processes are characterized by the theory of poroelasticity introduced by Biot (1941). Rice and Cleary (1976) have recast Biot's theory in terms of physical concepts. The equations governing the responses of fluid-infiltrated porous solids are expressed as:

$$\begin{aligned} 2G\varepsilon_{ij} &= \sigma_{ij} - \frac{v}{1+v}\sigma_{kk}\delta_{ij} + \frac{\alpha(1-2v)}{1+v}p\delta_{ij} \\ 2G\zeta &= \frac{\alpha(1-2v)}{1+v}\left(\sigma_{kk} + \frac{3}{B}p\right) \end{aligned} \tag{5}$$

where the indices take the values 1, 2 and 3 and repeated indices imply summation. The constitutive equations are expressed in terms of the total stress σ_{ij}, the pore pressure p, and their respective conjugate quantities, the solid strain ε_{ij} and variation of fluid volume per unit reference pore volume ζ. The basic material constants are the shear modulus G, the drained and undrained Poisson's ratios v and v_u and the Biot's effective stress coefficient α. B is the Skempton's pore pressure coefficient:

$$B = \frac{3(v_u - v)}{\alpha(1-2v)(1+v_u)} \tag{6}$$

Linear poroelastic processes are described by the constitutive equations, Darcy's law, the equilibrium equations and the continuity equations. A set of five material constants, G, v, v_u, α and κ, are needed to fully characterize a linear isotropic poroelastic system. These equations are combined into field equations in terms of u_i and p which consist of an elasticity equation with a fluid coupling term,

$$G\nabla^2 u_i + \frac{G}{1-2v}u_{k,ki} - \alpha p_{,i} = -F_i \tag{7}$$

and a diffusion equation with a solid coupling term,

$$\frac{\partial p}{\partial t} - \kappa M\nabla^2 p = -\alpha M\frac{\partial \varepsilon_{kk}}{\partial t} + M(\varphi - \kappa f_{i,i}) \tag{8}$$

where κ is the permeability coefficient, which is equal to k/μ, k is the intrinsic permeability, and μ is the fluid dynamic viscosity, φ is the source density (the rate of injected fluid volume per unit volume of the porous solid), $f_i = \rho_f g_i$ is the body force per unit volume of fluid, F_i is the body force per unit volume of the bulk material, and M is Biot's Modulus:

$$M = \frac{2G(v_u - v)}{\alpha^2(1-2v_u)(1-2v)} \tag{9}$$

The diffusion of pore pressure is coupled with the rate of change of the volumetric strain.

The response of a pressurized fracture can be obtained by superposition of two transient solutions corresponding to two nonzero boundary conditions on the fracture surface (Carter and Booker 1982). These two fundamental loading modes are

Mode 1

$$\begin{aligned} \sigma_n(x,y,z,t) &= -H(t), \\ p(x,y,z,t) &= 0; \end{aligned} \tag{10}$$

Mode 2

$$\begin{aligned} \sigma_n(x,y,z,t) &= 0, \\ p(x,y,z,t) &= H(t). \end{aligned} \tag{11}$$

where x, y, z correspond to the coordinates of the surface of the pressurized fracture, $H(t)$ denotes the heaviside step function. The initial conditions for both modes are stress free and zero pore pressure everywhere. Figure 1 illustrates the decomposed boundary conditions.

The responses of the model such as stress distribution, pore pressure distribution and aperture opening can be obtained in terms of response functions F_1 and F_2 for modes 1 and 2, respectively (Carter and Booker 1982; Detournay and Cheng 1991). Considering the existence of far-field stress S_0 normal to the fracture surface and pore pressure p_0 (Fig. 2), the response due to applied constant hydraulic pressure p_f can be found by superposition of the responses of mode 1 and mode 2:

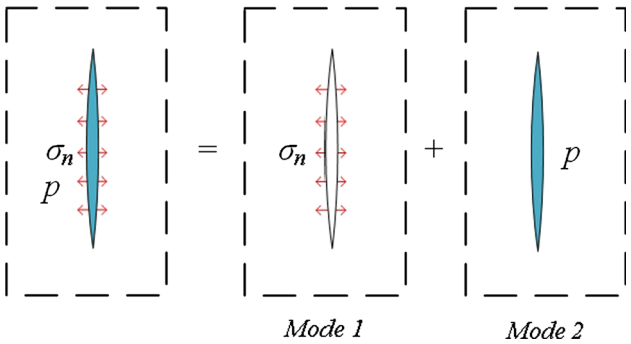

Fig. 1 Load decomposition for a pressurized fracture in a poroelastic rock: mode 1 (stress loading) is represented by a unit normal stress, σ_n, applied on the fracture surface; mode 2 (pore pressure loading) is represented by a unit pore pressure, p, (equal to σ_n) applied on the fracture surface

$$F = (p_f - S_0)F_1 + (p_f - p_0)F_2 \tag{12}$$

Following the Galerkin procedure and neglecting the existence of body forces, Eqs. (7) and (8) lead to the pair of equilibrium and continuity equations:

$$\begin{aligned} &[\mathbf{k}_\mathrm{m}]\{\mathbf{u}\} + [\mathbf{c}]\{\mathbf{p}_\mathrm{w}\} = \{\mathbf{f}\} \\ &[\mathbf{c}]^\mathrm{T}\left\{\frac{\partial \mathbf{u}}{\partial \mathrm{t}}\right\} - [\mathbf{k}_\mathrm{c}]\{\mathbf{p}_\mathrm{w}\} - [\mathbf{s}]\left\{\frac{\partial \mathbf{p}_\mathrm{w}}{\partial \mathbf{t}}\right\} = Q \end{aligned} \tag{13}$$

Linear interpolation in time using the Crank–Nicolson approximation yields:

$$\begin{bmatrix} \mathbf{k}_\mathrm{m} & \mathbf{c} \\ \mathbf{c}^\mathrm{T} & -(\mathbf{s} + \theta\Delta\mathrm{t}\mathbf{k}_\mathrm{c}) \end{bmatrix} \begin{Bmatrix} \Delta\mathbf{u} \\ \Delta\mathbf{p} \end{Bmatrix} = \begin{Bmatrix} \Delta\mathbf{f} \\ \Delta Q + \Delta\mathrm{t}\mathbf{k}_c\mathbf{p}_{\mathrm{t}_{n-1}} \end{Bmatrix} \tag{14}$$

where $\mathbf{u}$ and $\mathbf{p}$ are the vectors of the nodal displacements and nodal pore pressure. θ is the Crank–Nicolson approximation parameter, which is set to be 1 in this study so that the discretized equations are unconditional stable and numerical oscillations can be smoothed out (Smith and Griffiths 2004). Δt is the time step. $\Delta\mathbf{f}$ is the applied external force on nodes. ΔQ is the source/sink term. $\mathbf{p}_{t_{n-1}}$ is the nodal pore pressure component from the previous time step. Other matrices are presented as follows:

$$\begin{aligned} \mathbf{k}_\mathrm{m} &= \int B^T D B \mathrm{d}V \\ \mathbf{c} &= \int B^T \alpha m N_p \mathrm{d}V \\ \mathbf{s} &= \int N_p^T \frac{1}{M} N_p \mathrm{d}V \\ \mathbf{k}_\mathrm{c} &= \int (\nabla N_p)^T \kappa (\nabla N_p) \mathrm{d}V \end{aligned} \tag{15}$$

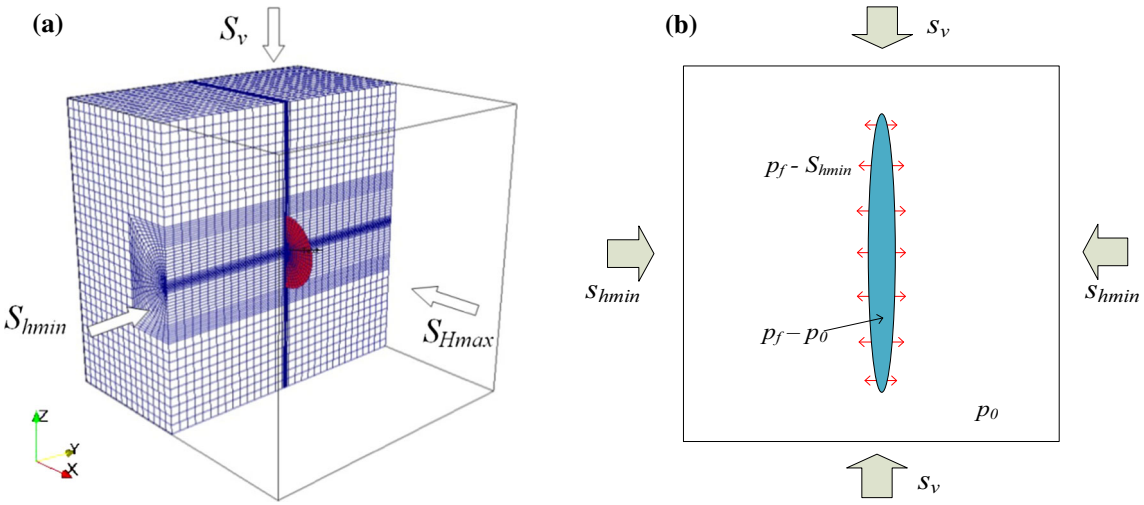

Fig. 2 A 3D mesh for the numerical simulation domain: **a** side view of the domain interior showing the circular fracture in *red*; **b** boundary conditions for the pressurized fracture in **a** showing a vertical section in the *yz*-plane (color figure online)

where $[D]$ is the material elastic matrix, $[B]$ is the strain–displacement matrix, $m = [1,1,1,0,0,0]^{\mathrm{T}}$, and $[N_{\mathrm{p}}]$ is the shape function for pore pressure.

3 Model Verification

A penny-shaped fracture under uniform pressurization in 3D domain is considered (Fig. 2). With appropriate change of the minor-to-major-axis ratio, an elliptic fracture or Griffith crack can be modeled. A uniform compressive stress and pore pressure field are initially assumed in the entire poroelastic domain. The initial minimum horizontal stress S_{hmin} is normal to the fracture surface. The initial pore pressure is p_0. At time $t = 0$, a constant pressure p_f is applied on the surface of fracture with a magnitude larger than S_{hmin}. The pressurized boundary of the fracture wall is decomposed into two nonzero boundary conditions as mentioned before.

To verify the poroelastic model, a fully loaded mode 1 penny-shaped fracture is modeled. The short- and long-term asymptotic profiles of the fracture aperture can be obtained according to the elastic solution (Sneddon 1946):

$$w(r) = \frac{2p_{\mathrm{net}}(1-v)R}{\pi G}\sqrt{1-\left(\frac{r}{R}\right)^2} \tag{16}$$

where p_{net} is the net pressure, which is defined as the treatment pressure minus the in situ minimum principal stress, equal to $p_f - S_{\mathrm{hmin}}$, R the radius of the fracture, v Poisson's ratio, G shear modulus, $w(r)$ fracture half width and r radial coordinate. Substituting undrained and drained Poisson's ratio into the above equation, the short- and long-term aperture profiles can be found. The short- and long-term responses give the bounding limits of the transient responses of the pressurized fracture (Rice and Cleary 1976). For the short-term ($t \approx 0$) response, a poroelastic medium behaves as an elastic material with the same shear modulus G and undrained Poisson's ratio v_{u}. The long-term ($t = \infty$) response is represented by an elastic response with the drained Poisson's ratio v.

Figure 3 shows the mode 1 (stress loading) transient fracture opening profiles. Dimensionless time $t^* = ct/R^2$ is used for transient evolution of the fracture profile. For comparison, an elastic FEM simulation using a drained Poisson's ratio is also included. As illustrated in the figure, the FEM poroelastic results approach these asymptotic limits (short- and long-term responses). The long-term poroelastic results overlap with the elastic solution using drained Poisson's ratio. A single curve is formed when each of the fracture profiles is normalized by their maximum values (Fig. 4). The transient poroelastic responses of the pressurized fracture agree well with the asymptotic

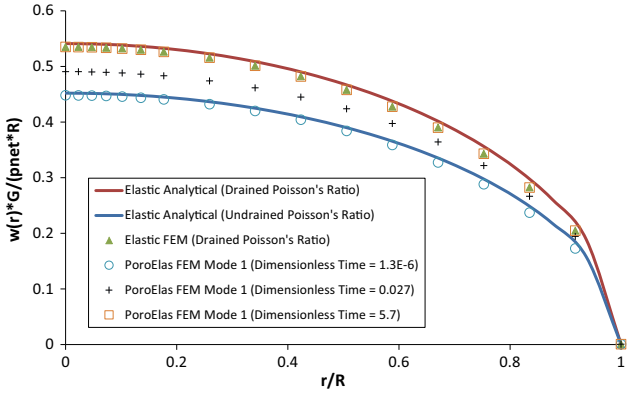

Fig. 3 Fracture width versus radial distance for a penny-shaped fracture under mode 1 (or stress) loading. Comparison of numerical and analytical results for elastic and poroelastic cases. The very short-time poroelastic results correspond to undrained rock response. The long-term poroelastic results correspond to drained response which equal that of a purely elastic rock

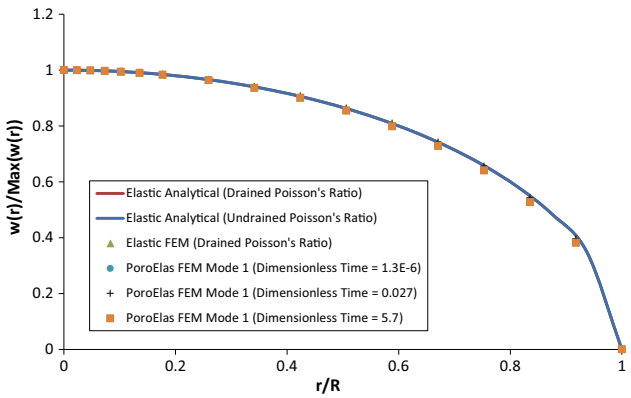

Fig. 4 Normalized mode 1 fracture width versus radial distance for a penny-shaped fracture. The profile of the normalized fracture aperture is independent of time and material properties

solutions calculated based on Eq. (16), which verifies the applicability of the presented poroelastic model and its corresponding FEM implementation.

4 Numerical Simulations

In the following sections, the total response of the poroelastic model is found by a linear combination of the responses of mode 1 (stress loading) and mode 2 (pore pressure loading) according to Eq. (12). Homogeneous elastic properties are first considered. Then the analysis is extended to more general heterogeneous scenarios.

4.1 Homogeneous Case

The opening of the fracture and the poroelastic effects during hydraulic stimulation induce stresses around the

Table 1 Basic input parameters for the homogeneous case

Geometry of models	640 × 800 × 640 m (length/width/height)
Poisson's ratio, v	0.15
Undrained Poisson's ratio, v_u	0.29
Biot's effective stress coefficient, α	0.7
Young's modulus, E (homogeneous case)	2.76×10^{10} Pa
Permeability (homogeneous case), k	5.0 md
Fluid dynamic viscosity, μ	2.0×10^{-4} Pa s
Initial stress state	
Vertical stress, S_v	41 MPa
Max. hori. stress, S_{Hmax}	33 MPa
Min. hori. stress, S_{hmin}	29 MPa
Initial pore pressure, P_0	18 MPa
Net pressure, $P_f - S_{hmin}$	7 MPa

stimulated region (Ghassemi et al. 2013; Rawal and Ghassemi 2011; Safari and Ghassemi 2015). Consider that a penny-shaped fracture in a rock with mechanical properties of Weber sandstone (Rice and Cleary 1976) is uniformly pressurized. The radius of the fracture is 80 m, and the basic input parameters for the homogeneous case are listed in Table 1. We assume the stress gradients are 1.0 psi/ft for S_v, 0.8 psi/ft for S_{Hmax}, 0.7 psi/ft for S_{hmin}, and the fluid pressure gradient is 0.433 psi/ft, yielding the values listed in Table 1 for a depth of 6000 ft.

Figure 5 illustrates the induced total stress and pore pressure distributions along a line (OA) perpendicular to the fracture surface passing through the center of the fracture. On the fracture surface, the fluid pressure (P_f) is kept at 36 MPa; the induced fluid pressure ($\Delta P = P_f - P_0$) is 18 MPa, based on the assumption that $P_f = P_{net} + S_{hmin}$ on the fracture surface; the induced minimum horizontal stress (ΔS_{yy}) is maintained at 7 MPa, which is equal to the applied net pressure. At the beginning of pressurization ($t = 0.02$ s and $t = 7$ min), the induced pore pressure (ΔP) is larger than the induced horizontal and vertical stresses (ΔS_{xx}, ΔS_{yy} and ΔS_{zz}) on the fracture surface; the induced pore pressure (ΔP) is less than the induced minimum horizontal stress (ΔS_{yy}) from where L/R > 0.4. As time goes by, the pore pressure gradually diffuses further into the formation. When $t = 24$ h, the induced pore pressure is larger than the induced horizontal and vertical stresses (ΔS_{xx}, ΔS_{yy} and ΔS_{zz}) in the entire numerical domain.

The shear stresses are shown in Fig. 6 and are close to zero in the homogeneous poroelastic rock during the entire process of pressurization. The oscillations in Fig. 6b, c are of the magnitude of 10^{-13} MPa and can be considered as numerical error.

Figure 7 illustrates the orientations of the minimum principal stresses at $t = 7$ min and $t = 24$ h. Black lines indicate the directions of the minimum principal stress at

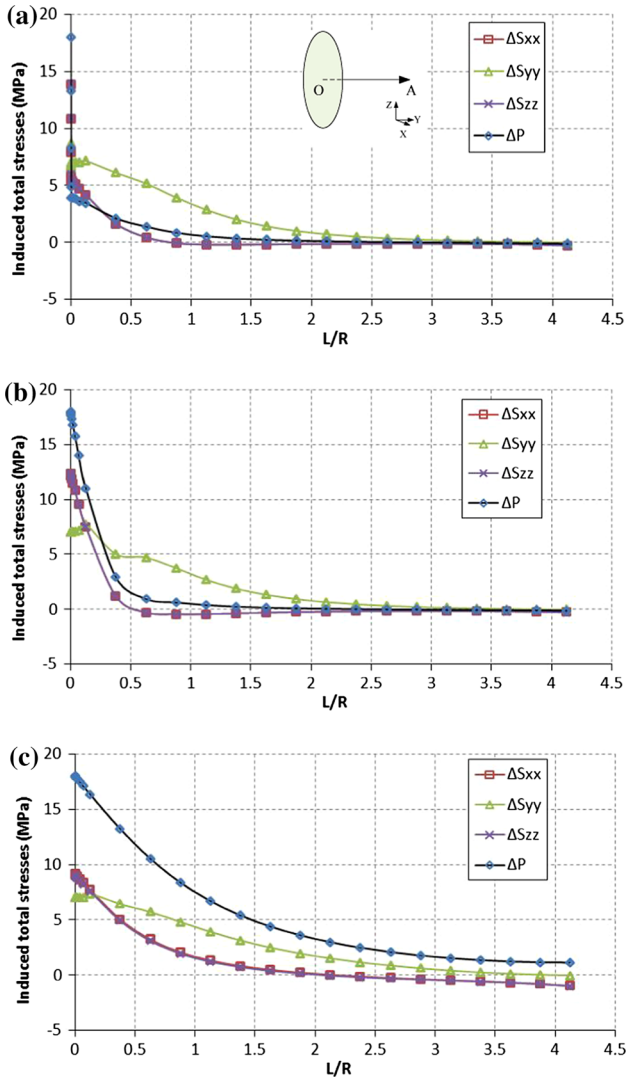

Fig. 5 Induced total (sum of mode 1 and mode 2) stresses and pore pressure along a line (OA) (*top figure*) perpendicular to the fracture surface, passing through the center of the fracture: **a** $t = 0.02$ s; **b** $t = 7$ min; **c** $t = 24$ h

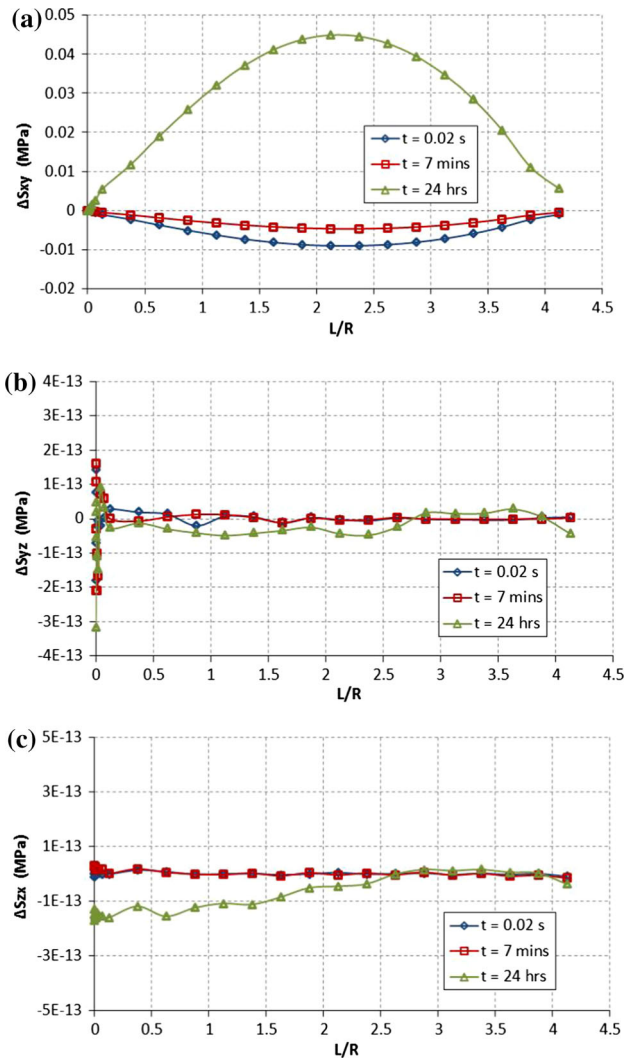

Fig. 6 Induced (total) shear stresses along the line OA (see Fig. 5a) perpendicular to the fracture surface passing through the center of the fracture: **a** ΔS_{xy}; **b** ΔS_{yz}; **c** ΔS_{zx}

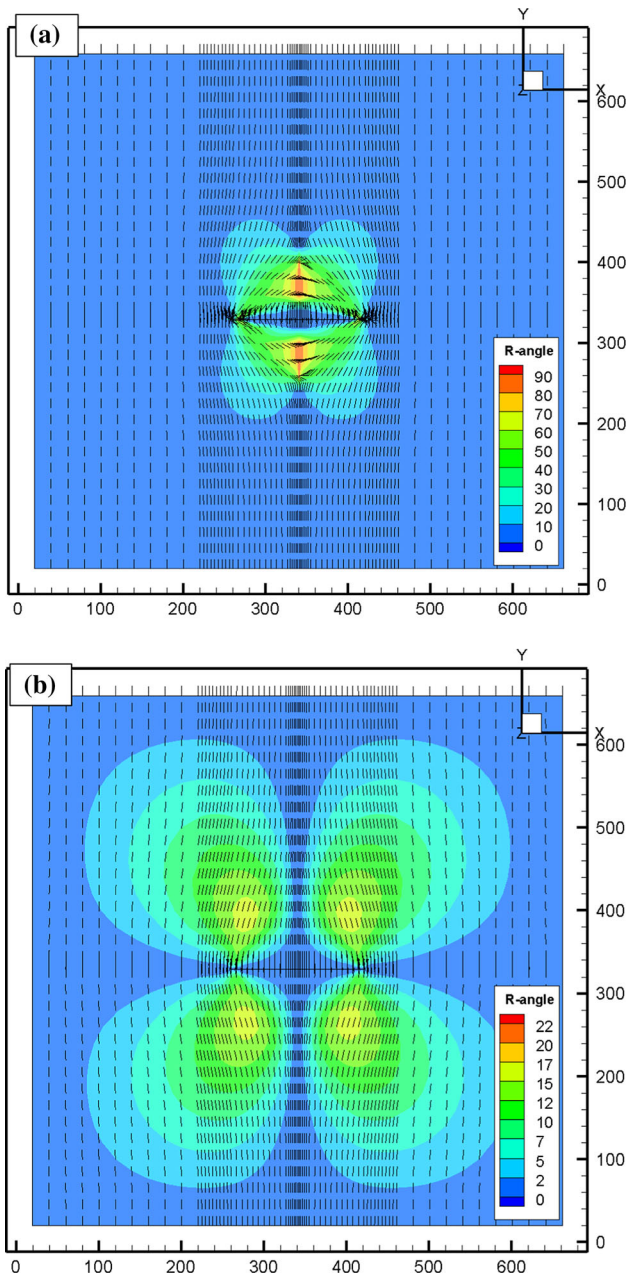

Fig. 7 Symmetrical distributions of reorientation angle (R-angle) of the minimum principal stress in a plane cut through the center of the fracture (the central plane parallel to the XY plane in Fig. 2): **a** $t = 7$ min; **b** $t = 24$ h. The small dashes indicate the orientation of the minimum principal stress at those locations (color figure online)

points within the domain. The color contour represents the rotation angle of the minimum principal stresses from their original orientations and is symmetric to the pressurized fracture (due to the symmetric boundary conditions adopted here). As can be seen, stress-reversal regions develop, where the minimum principal stresses rotate 90°, exist at $t = 7$ min in the areas extended away from the fracture surface. This phenomenon is consistent with Fig. 5b and will be analyzed in the Discussion section. After 24 h of pressurization, no stress-reversal regions exist. The maximum rotation angle is around 30°. The regions with relatively a large rotation angle are close to the fracture tips where the stress singularity exists.

As can be seen from Fig. 5, the induced stress component in the y-direction (direction of the initial minimum horizontal stress) is always larger than the component in the x-direction (direction of the initial maximum horizontal stress) and the extent of the region of stress reorientation and stress reversal (stress reversal indicates that the principal stresses rotate 90°) largely depends on the initial in situ stress contrast and the applied net pressure. When the initial in situ stress contrast ($S_{xx} - S_{yy}$) is larger than the generated stress contrast ($\Delta S_{yy} - \Delta S_{xx}$), which is a function of net pressure, the minimum principal stress is still in the y-direction and there is no stress reversal in the vicinity of the fracture surfaces. However, a reoriented

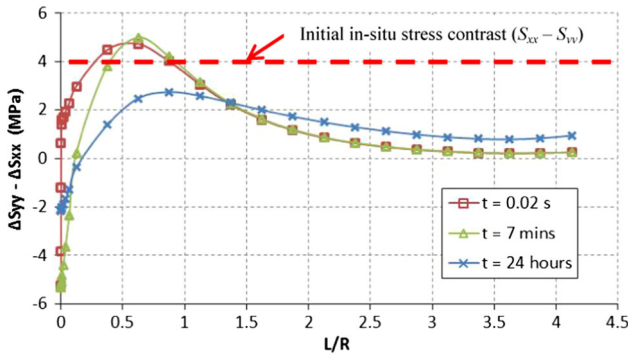

Fig. 8 Generated stress contrast ($\Delta S_{yy} - \Delta S_{xx}$) at different pressurization time along the line OA (see the top of Fig. 5) through the center of the fracture and perpendicular to it (homogeneous rock scenario)

stress region exists around the fracture tips. The generated stress contrast ($\Delta S_{yy} - \Delta S_{xx}$) is shown in Fig. 8. The red dashed line in Fig. 8 indicates the initial in situ stress contrast ($S_{xx} - S_{yy}$). At $t = 0.02$ s and 7 min, we have $(\Delta S_{yy} - \Delta S_{xx}) > (S_{xx} - S_{yy})$, so stress-reversal regions exist in areas extending away from the fracture surface (Fig. 7a). At $t = 24$ h, there are no stress-reversal regions $((\Delta S_{yy} - \Delta S_{xx}) < (S_{xx} - S_{yy}))$ as pore pressure diffuses further into the formation. The stress-reversal phenomenon is discussed further in the Discussion section.

4.2 Heterogeneous Case

As mentioned before, five material constants are needed to fully characterize a linear isotropic poroelastic system. In this work, we use E, ν, ν_u, α and κ for this purpose. Each of these parameters and their combinations can be considered as randomly distributed variables in the poroelastic model. As we know, flooding a porous rock will cause it to expand. When the expansion is constrained, a confining pressure is generated as a function of α and ν (Cheng et al. 1993). Thus, nonuniform distributions of α and ν can generate heterogeneous stress fields. Also, the variation of Young's modulus alters the stiffness matrix in stress–strain relationship so the calculated stresses also experience alterations. The long-time response ($t = \infty$) of a poroelastic rock is similar to the response of an elastic material with drained Young's modulus and Poisson's ratio. The undrained moduli control the rock behavior during short times ($t \approx 0$).

To illustrate the influence of heterogeneity, example simulations using Young's modulus and permeability as random variables are presented and discussed in detail. The same procedure could be used with other parameters treated as random variables. Lognormal distribution is adopted here. Statistical values for the assumed random variables are presented in Table 2. Figures 9 and 10 show the 3D

Table 2 Statistical values for the assumed random variables

	Young's modulus (Pa)	Permeability (md)
Input data		
Mean value	2.76E+10	5.00
Variation value	5.52E+09	1.00
Output data		
Arithmetic average	2.74E+10	4.95
Geometric average	2.71E+10	4.90
Harmonic average	2.67E+10	4.84
Max. value	4.87E+10	8.83
Min. value	1.42E+10	2.57

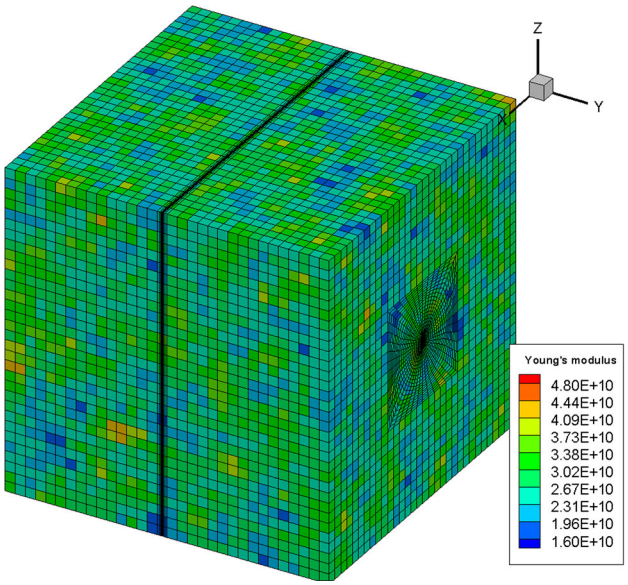

Fig. 9 Random distribution of Young's modulus (Pa)

random distributions of the Young's modulus and permeability, respectively.

Figure 11 illustrates the induced total stresses and pore pressure along a line perpendicular to the fracture surface, passing through the center of the fracture. Comparison with Fig. 5 shows that the normal stresses in heterogeneous rock (Young's modulus and permeability heterogeneity) have almost the same distributions as those in homogeneous rock. The shear stresses are given in Fig. 12. As can be seen, they are one order of magnitude larger than those in the homogeneous case. When the shear stress components (S_{xy}, S_{yz}, S_{zx}) are negligible compared to normal stresses components (S_{xx}, S_{yy}, S_{zz}), the normal stresses are also principal stresses. In the heterogeneous case, the induced shear stresses cause the directions of local principal stresses to become heterogeneous [see the reorientation of the minimum principal

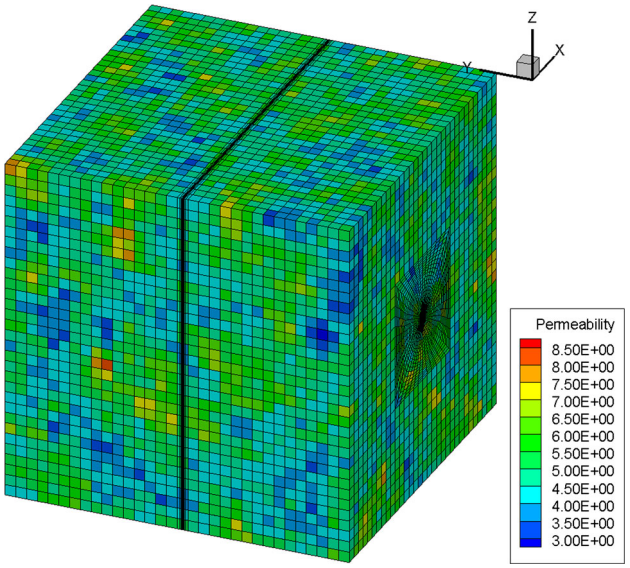

Fig. 10 Random distribution of permeability (md)

stress (Fig. 13)]. In the homogeneous case, the deformation of the model is uniform so no shear stresses (or very small shear stresses) are generated. The shear stresses are generated primarily where different materials come into contact (material interfaces). The higher the contrast of material properties along the interface, the larger the generated shear stresses. We will discuss these phenomena in the following section. In addition, the fluctuation of shear stresses is a function of time and is thus related to the diffusion of pore pressure. This is shown in Fig. 12 for shear stresses at $t = 0.02$ s, $t = 7$ min and $t = 24$ h, respectively.

Initially, the minimum principal stress is the horizontal stress (S_{yy}). The black lines in Fig. 13 show the directions of the minimum principal stresses located in a horizontal plane. After applying hydraulic pressure to the fracture surfaces, we can observe that some regions of the horizontal plane do not have black lines. This indicates that in certain areas the minimum principal stresses are no longer horizontal. In the homogeneous case, the minimum principal stresses remain in the horizontal direction everywhere, although they rotate by a certain angle depending on the position with respect to the pressurized fracture (Fig. 7). The contours in Fig. 13 illustrate the rotation angle of minimum principal stresses in the horizontal plane. The value of the rotation angle has a complex distribution and is not symmetric with respect to the pressurized fracture. The rotation angle gradually decreases as time elapses, due to the diffusion of pore pressure into the formation, which causes the induced stress contrast ($\Delta S_{yy} - \Delta S_{xx}$) to gradually decrease as shown in Fig. 8.

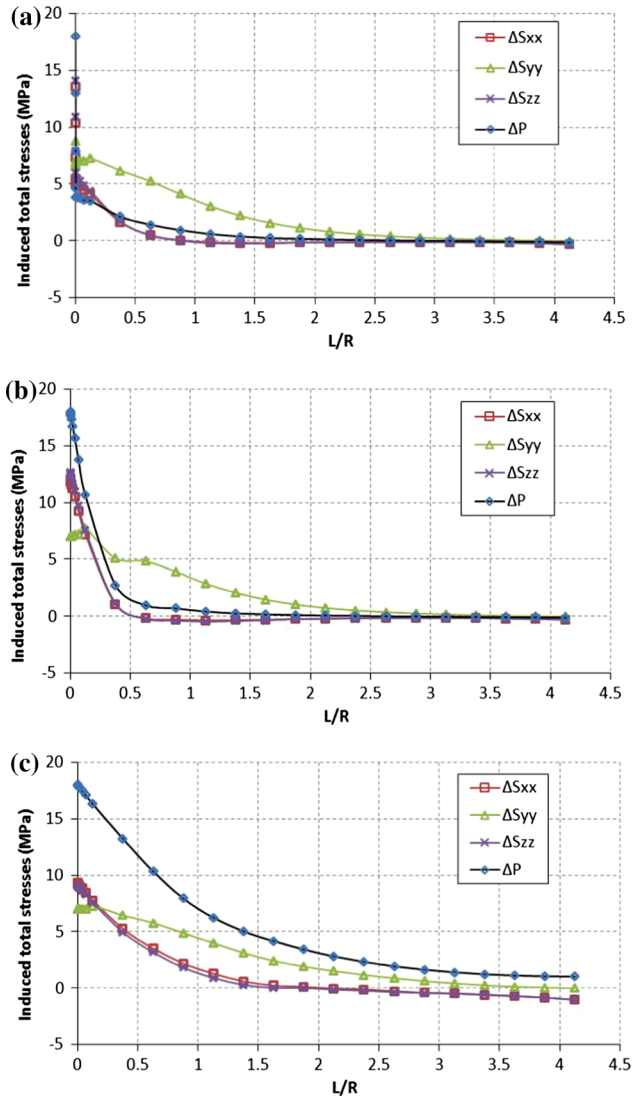

Fig. 11 Induced total stresses and pore pressure along the line OA (see Fig. 5a) perpendicular to the fracture surface, passing through the center of the fracture, for the heterogeneous case: **a** $t = 0.02$ s; **b** $t = 7$ min; **c** $t = 24$ h

5 Discussion

The importance of understanding stress redistributions during hydraulic stimulation lies in the fact that stresses predominantly control the fracture propagation. Much effort has been devoted to the analyses of stress redistribution around a hydraulic fracture based on the assumption of homogeneous rock properties, ignoring the inherently heterogeneous nature of unconventional reservoirs. As has been demonstrated in previous sections, stress redistributions (magnitude and direction) in heterogeneous poroelastic rocks are much different from those in homogeneous systems. Although the normal stress components in the two different cases are nearly the same, the shear stresses are larger and are nonuniformly distributed in the

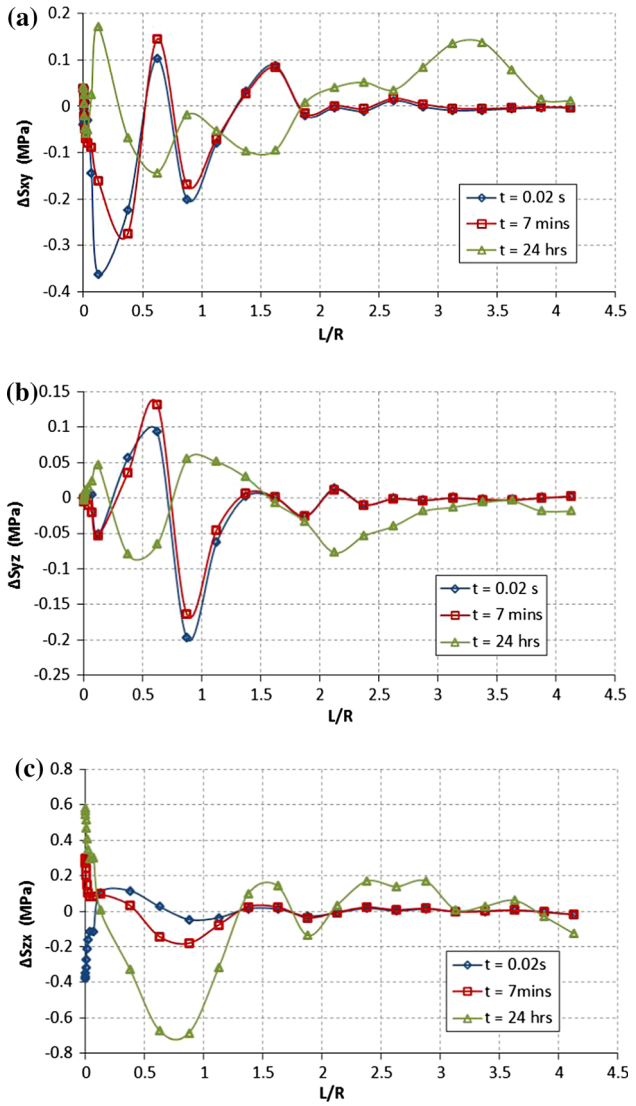

Fig. 12 Variation of induced shear stresses along the line OA (see Fig. 5a) perpendicular to the fracture surface, passing through the center of the fracture, for the heterogeneous case: **a** S_{xy}; **b** S_{yz}; **c** S_{zx}

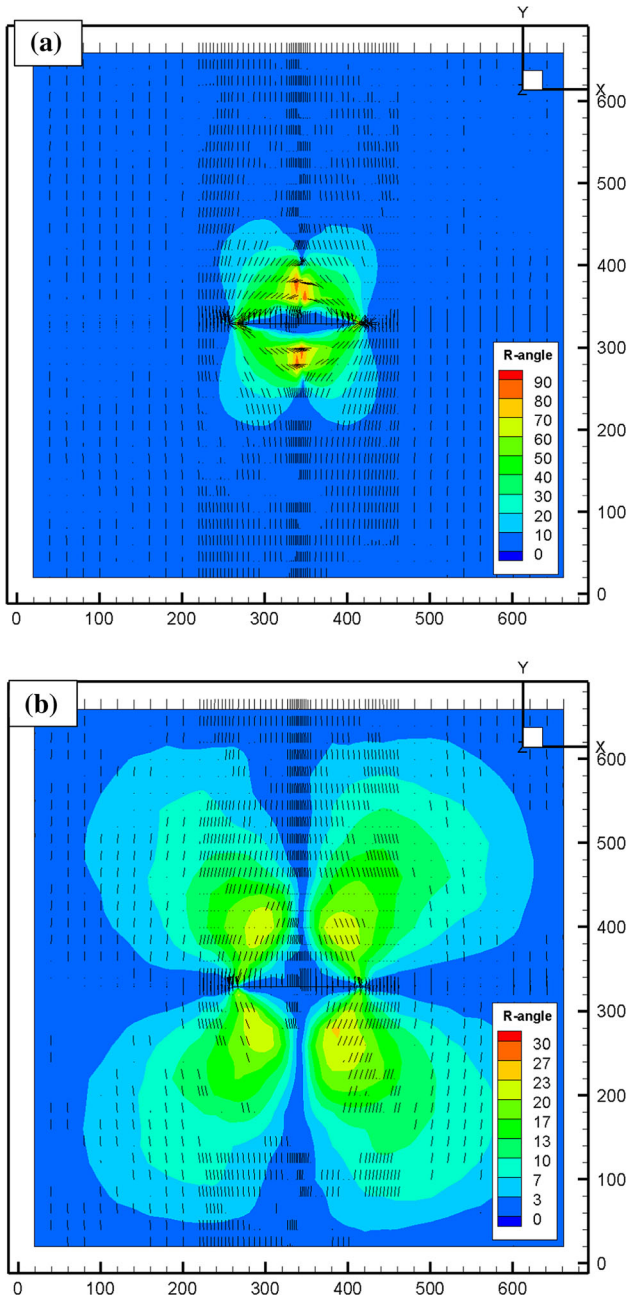

Fig. 13 Unsymmetrical distributions of reorientation angle (R-angle) of the minimum principal stress for the heterogeneous medium from a top view slice cutting through the center of the fracture: **a** $t = 7$ min; **b** $t = 24$ h

heterogeneous case (Fig. 12). The reasons for the observed trends can be explained using relatively simple simulations as described below.

5.1 Influence of Young's Modulus

Consider a 1.2 m × 1.2 m × 1.2 m cube of rock as shown in Fig. 14. An interior cubical subregion of size 0.6 m × 0.4 m × 0.6 m (interior zone) is considered to have poroelastic properties different from the rest of the larger cube (exterior zone). Then, the left side of the cube is subjected to a fluid pressure of 36 MPa with the traction acting in the y-direction (Fig. 14b). The solid and fluid displacements are set to zero on all other boundaries. The whole simulation domain is divided into cubic elements of size 0.1 m (Fig. 14). The material properties used for the exterior elements are the same as those used in the homogeneous case (Table 1), while the properties of the interior zone are varied and the resulting stress and pore pressure distributions are simulated. To evaluate the influence of Young's modulus on the resulting stresses, we lower the elastic properties of the interior cubical subregion during different simulation runs such that the Young's modulus ranges from an initial base case value of

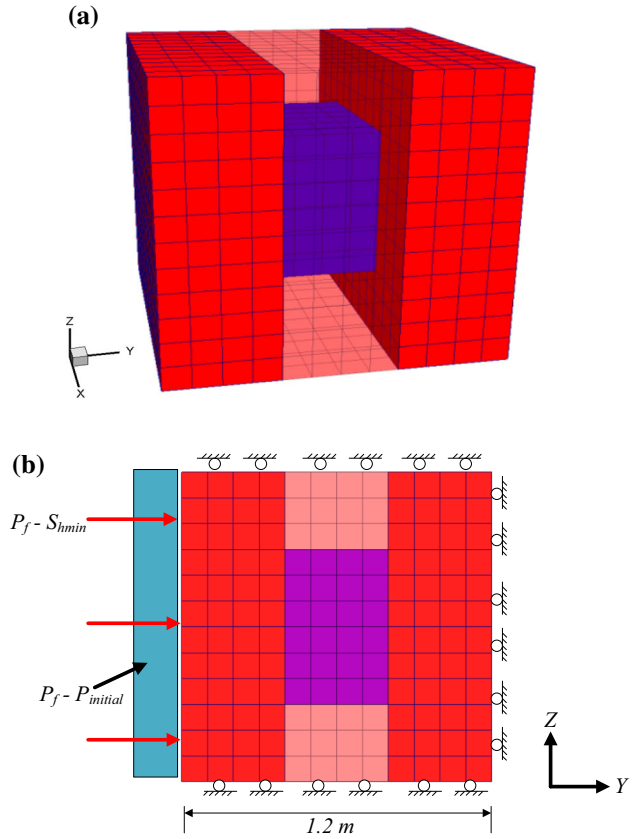

Fig. 14 **a** A 3D model of a simple heterogeneous system showing a cube or rock with an interior zone having different properties than the rest of the body. Elements with different Young's modulus are shown in *purple* (interior zone). *Red color* indicates the exterior zone; **b** a section of the 3D model showing the central section parallel to the *yz*-plane and the boundary conditions (color figure online)

2.76×10^{10} Pa to 90, 70, 50, 30 and 10% of the base case value. For the elements in the exterior zone, the Young's modulus is kept at the initial value.

The following results are obtained at $t = 7$ min (the small model reaches steady state after 7 min of pressurization with a uniform pore pressure of 36 MPa). Figure 15 shows the displacements in the *x*- and *y*-direction on the central horizontal plane. In the case shown, the Young's modulus of the elements in the central part (marked by the red dashed lines) is 50% of that for the surrounding elements providing for a larger mode 2 response (dilation) in the interior zone. As expected, the displacement field (and strain) is not uniform. The elements with a lower Young's modulus tend to contract more in the *x*-direction (due to the system dilation in the *y*-direction in response to the pore pressure increase). The same phenomenon exists for displacement in the *xz*-plane because the material properties are symmetrically distributed (with respect to the *y*-axis).

Figure 16 shows the distribution of induced shear stresses ΔS_{xy} on two orthogonal planes. Induced shear

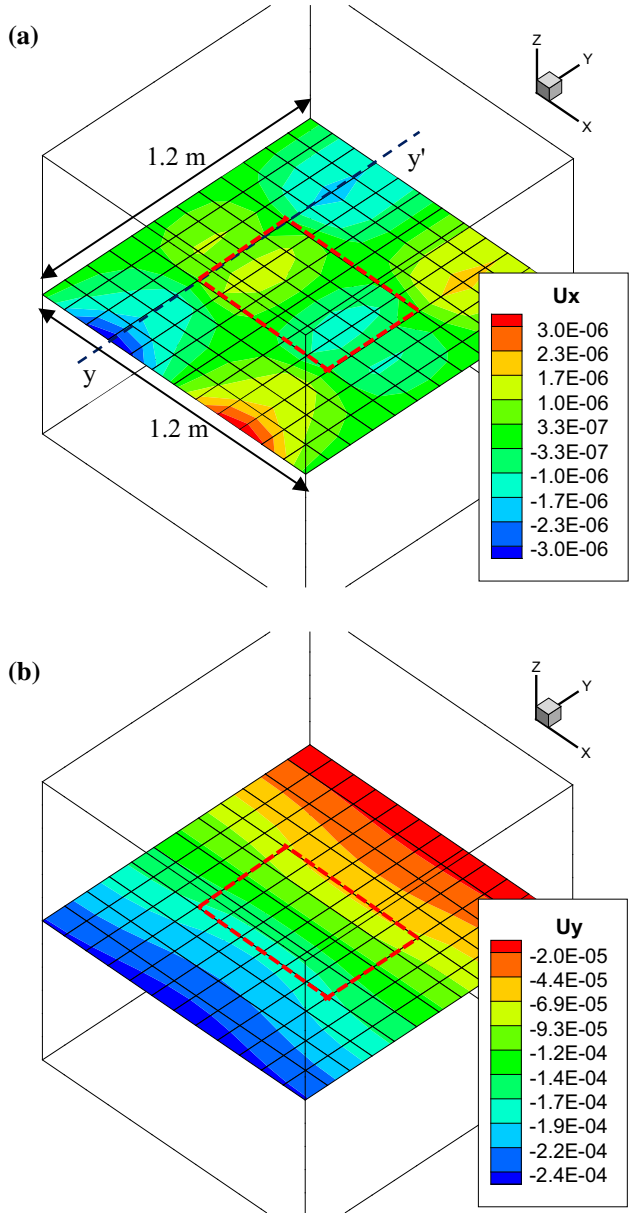

Fig. 15 Displacements in *x*- and *y*-direction on a central horizontal plane: **a** displacement in *x*-direction; **b** displacement in *y*-direction (area encircled by *red dash lines* has 50% of initial Young's module.) (unit: m) (color figure online)

stresses, ΔS_{xy}, are observed at the interface separating zones with different Young's modulus.

Sensitivity analyses on the effects of Young's modulus are presented next. Six different scenarios are considered. In the base case, the same Young's modulus values are assigned to the exterior and interior zones. In the other five scenarios, the interior zone has a Young's modulus equal to 10, 30, 50, 70 and 90% of the base case. The induced total normal and shear stresses along the line yy' (illustrated in Fig. 16) are presented in Figs. 17 and 18, respectively.

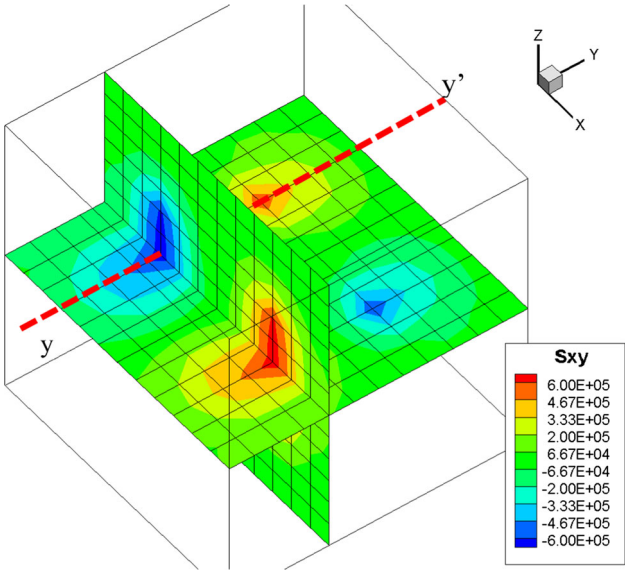

Fig. 16 Distribution of ΔS_{xy} on two orthogonal slices (unit: Pa)

The elements with smaller Young's moduli are located from 0.4 to 0.8 m along the line yy'. The induced stress components ΔS_{xx}, ΔS_{yy} and ΔS_{zz} show variations between $y = 0.4$ and 0.8 m. The maximum variations for ΔS_{xx}, ΔS_{yy} and ΔS_{zz} are 0.7, 0.6 and 1 MPa, respectively. Because of the change of Young's modulus at these locations, the deformation is nonuniform (Figs. 15, 19). The magnitudes of the variations are usually less than 1 MPa, even for the extreme scenario ($E_{\text{weak}}/E_{\text{original}} = 0.1$), which are rather small when compared with their values in the base case.

The magnitude of the induced shear stress, ΔS_{xy}, varies in the range of 0.5–2 MPa between $y = 0.4$ m and $y = 0.8$ m. For S_{yz} and S_{zx}, the variations are close to zero. Due to the symmetric distribution of material properties with respect to the y-axis, the stress distributions along lines parallel to the y-direction exhibit the same patterns.

From Fig. 19, it is observed that displacements in the x-direction along the line yy' are negative except at $y = 0.4$ m and $y = 0.8$ m, where the two corners of the weak zone (Fig. 15) are located. However, as can be seen from Fig. 15a, the x-displacements in the weak zone are in the positive x-direction beyond the line yy' and the weak zone is contracting during pressurization. The net response (mode 1 plus mode 2) is a contraction because of the relatively larger dilation in the y-direction toward the loaded surface due to pore pressure increase.

The distributions of the induced total stress ΔS_{yy} on a central horizontal plane are presented in Fig. 20 for mode 1, mode 2 and mode 1 + 2. The interior weak zone encircled by the red dashed lines has a Young's modulus equal to 50% of the surrounding elements. For the homogeneous distribution of Young's modulus, the induced

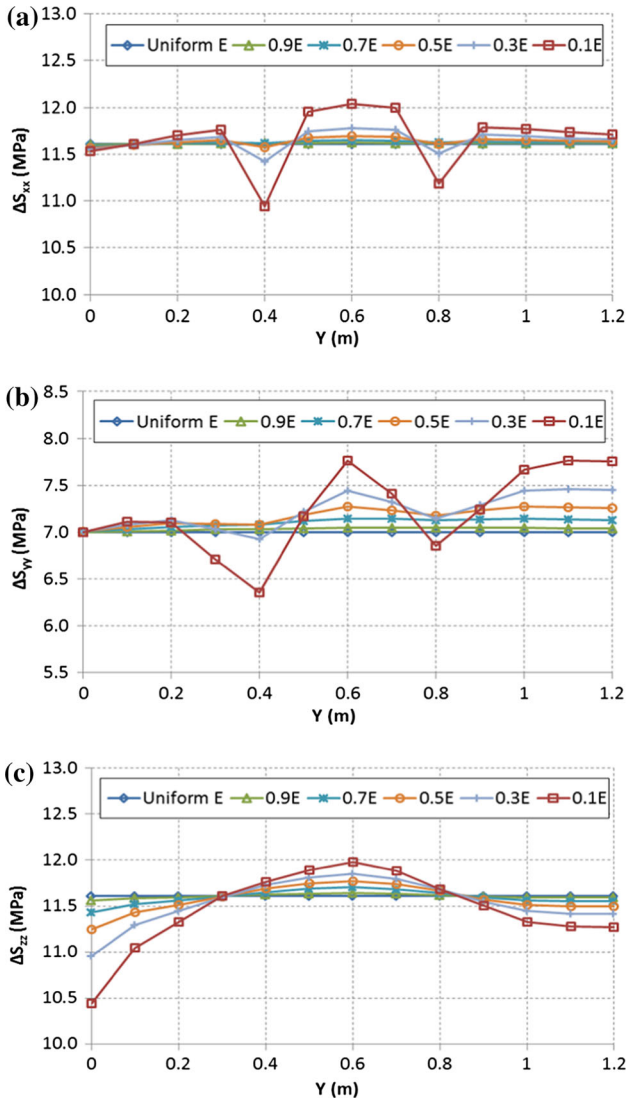

Fig. 17 Induced normal stresses along the line yy' for cases with different Young's modulus between $y = 0.4$ m and $y = 0.8$ m: **a** ΔS_{xx}; **b** ΔS_{yy}; **c** ΔS_{zz}

stresses are distributed uniformly in the entire domain, as illustrated in Figs. 17, 18 and 19 for the case with uniform E. In the heterogeneous case, mode 1 loading generates smaller induced total stress component ΔS_{yy} in the weak zone compared with the induced stresses in exterior elements; mode 2 has larger ΔS_{yy} in the weak zone. Combining mode 1 and mode 2, we observe from Fig. 20c that the interior weak zone has a larger ΔS_{yy}. We notice from Fig. 15 that the weak zone is under contraction in the x-direction during pressurization. These behaviors are different from those of an elastic (in contract to poroelastic) medium, which only act like mode 1 loading.

Because of the spatial variation of Young's modulus, nonuniform deformations and shear stresses are generated at material interfaces. In addition to the change of mechanical properties, such as Young's modulus,

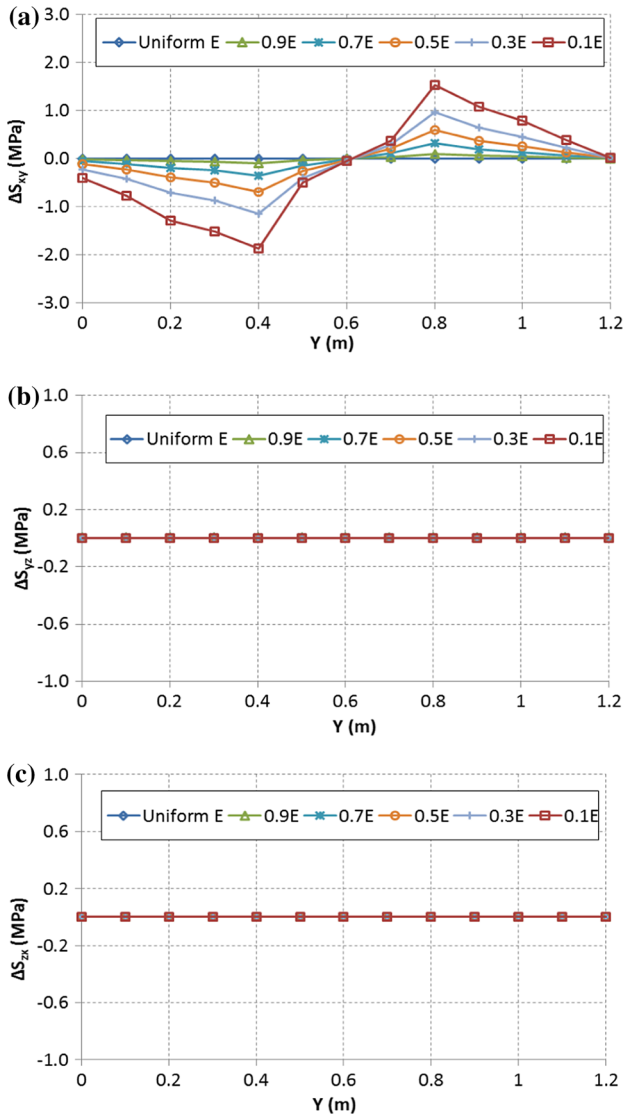

Fig. 18 Induced shear stresses along the line yy' for cases with different Young's modulus between $y = 0.4$ m and $y = 0.8$ m: **a** ΔS_{xy}; **b** ΔS_{yz}; **c** ΔS_{zx}

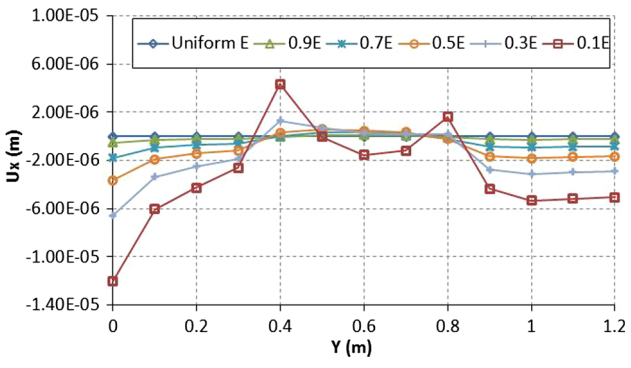

Fig. 19 Displacement in x-direction along the line yy'

discontinuities (e.g., natural fractures) can also induce heterogeneous stress redistributions when their mechanical properties are different from their surrounding materials. This simple example illustrates some underlying physical processes that lead to the complex stress response observed in the stress field around a pressurized crack considered in the previous section.

5.2 Influence of Biot's Effective Stress Coefficient

Instead of altering the Young's modulus, consider gradually changing Biot's effective stress coefficient, α, from 0.1 to 0.9 for the elements in the central region while keeping that of the surrounding elements equal to 0.5. Figure 21 illustrates the total normal stresses along the line yy'. The value in the legend indicates α for the elements in the central zone. As can be seen, the normal stresses are increased for larger α and decreased for smaller α. The variations of ΔS_{xx}, ΔS_{yy} and ΔS_{zz} are in the range of 1.5–3, 0.5–0.8 and 1–2 MPa, respectively. Injection into a porous medium causes it to dilate (Cheng et al. 1993). When the expansion is constrained, confining stresses will be generated as a function of Biot's effective stress coefficient:

$$\Delta S_{xx} + \Delta S_{yy} + \Delta S_{zz} = -\frac{2\alpha(1-\nu)}{1-\nu}\Delta p \tag{17}$$

The induced stresses vary in different zones when α changes from one zone to another.

In addition to the induced stress variations, the induced displacements also vary in different zones and at the interfaces of the materials with different α. The displacement component in the x-direction along the line yy' is plotted in Fig. 22; it can be seen that it has a uniform distribution when $\alpha = 0.5$. When $\alpha > 0.5$ for elements in the central zone, it tends to expand; when $\alpha < 0.5$, it tends to contract. These are consistent with the changes of normal stresses. Figure 23 shows the shear stress distributions along the line yy'. Shear stresses in the range of 1 MPa $\sim$ 2 MPa develop along the interfaces of materials with different α.

5.3 Influence of Drained and Undrained Poisson's Ratio

According to Eq. (17), the induced normal stresses are also a function of drained Poisson's ratio, ν. The range for ν is $0 \le \nu \le \nu_u$. If we assume $\nu = 0.25$ for the elements in the central part of the model and $\nu = 0.15$ for the surrounding elements, the maximum variations of normal and shear stresses are 0.3 MPa and 0.2 MPa, respectively. When the diffusion of fluid pressure reaches a steady state in a

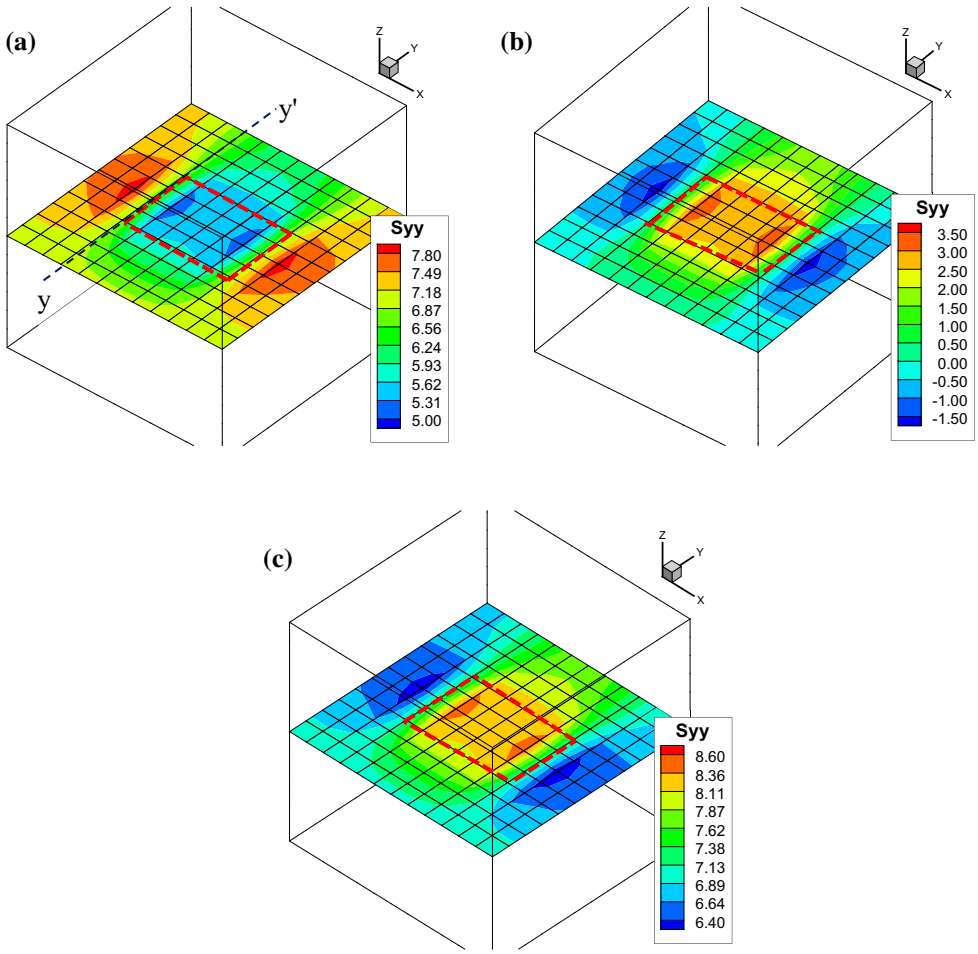

Fig. 20 Induced total stress ΔS_{yy} (compression positive) on a central horizontal plane: **a** mode 1; **b** mode 2; **c** mode 1 + 2 (unit: MPa)

poroelastic rock, the rock's mechanical response is the same as that of an elastic material with the same drained Poisson's ratio. The undrained Poisson's ratio influences the poroelastic behavior in transient states. The range of undrained Poisson's ratio values is relatively small. Assuming $\nu_u = 0.4$ for the elements in the central zone of the model and $\nu_u = 0.29$ for the surrounding elements, the maximum perturbations of normal and shear stresses at $t = 0.02$ s are 0.6 and 0.2 MPa, respectively, so that the difference in the induced stresses at material interfaces are small.

An interesting phenomenon is illustrated in Fig. 8. The induced stress contrast ($\Delta S_{yy} - \Delta S_{xx}$) due to pressurization of the fracture is less than the original in situ horizontal stress difference in a region close to the fracture surface (in this case L/R < 0.3). This indicates that the maximum horizontal stress, S_{xx}, will always be larger than the minimum horizontal stress, S_{yy}; there will be no stress reversal in regions close to the fracture surface. This is in contrast to predictions that are based on an elastic formulation without consideration of the pore pressure diffusion effects on rock deformation (and stresses). In an elastic solution to the problem, ΔS_{xx} is always less than ΔS_{yy}, so that ($\Delta S_{yy} - \Delta S_{xx}$) > 0 causing the principal stresses to rotate by 90° provided that the induced stress contrast is larger than the background in situ stress contrast, $S_{xx} - S_{yy}$.

The induced stress contrast, $\Delta S_{yy} - \Delta S_{xx}$, on fracture surface in a poroelastic rock can also be estimated from the solution to the 1D problem (Fig. 24) of fluid pressure loading of an infinite half-space (Cheng 2016). The pressure loading condition can also be decomposed into modes 1 and 2. Using the analytical solution for the 1D fluid pressure loading with the same parameters as in Table 1, the induced stresses are obtained and plotted in Fig. 25. As can be seen, the induced stress contrast, $\Delta S_{yy} - \Delta S_{xx}$, on the pressure loading surface is -5 MPa, which is almost the same as our numerical results for pressurized penny-shaped fracture when $t = 0.02$ s and $t = 7$ min.

Rocks generally exhibit heterogeneous and anisotropic characteristics. Both of these characteristics could influence the stress and pore pressure distributions during hydraulic fracturing. Our current model can be used to generate heterogeneous isotropic parameters. The role of anisotropic rock properties on hydraulic fracturing has been considered in Sesetty and Ghassemi (2016). More effort is needed to improve the model of this paper to consider rock anisotropy and is left for future work. In real

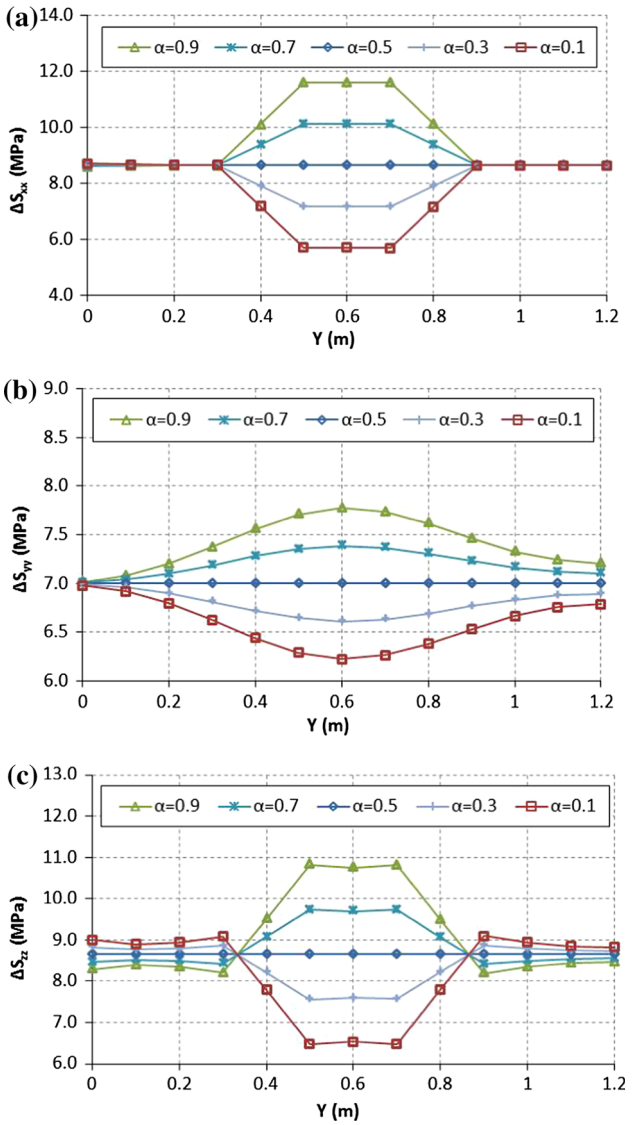

Fig. 21 Induced normal stresses along the line yy' (see Fig. 20) due to the change of Biot's effective stress coefficient, α, between $y = 0.4$ m and $y = 0.8$ m: **a** ΔS_{xx}; **b** ΔS_{yy}; **c** ΔS_{zz}

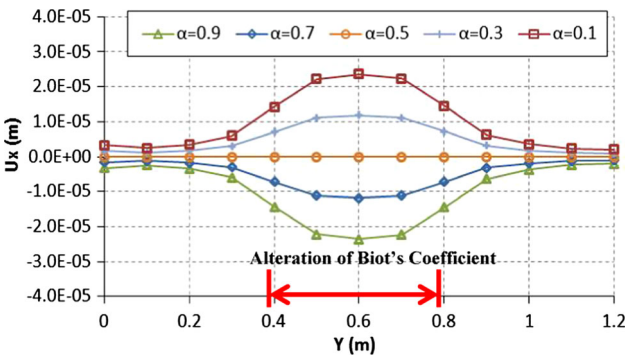

Fig. 22 Displacement in the x-direction along the line yy' (see Fig. 20) for different Biot's effective stress coefficients in the central zone

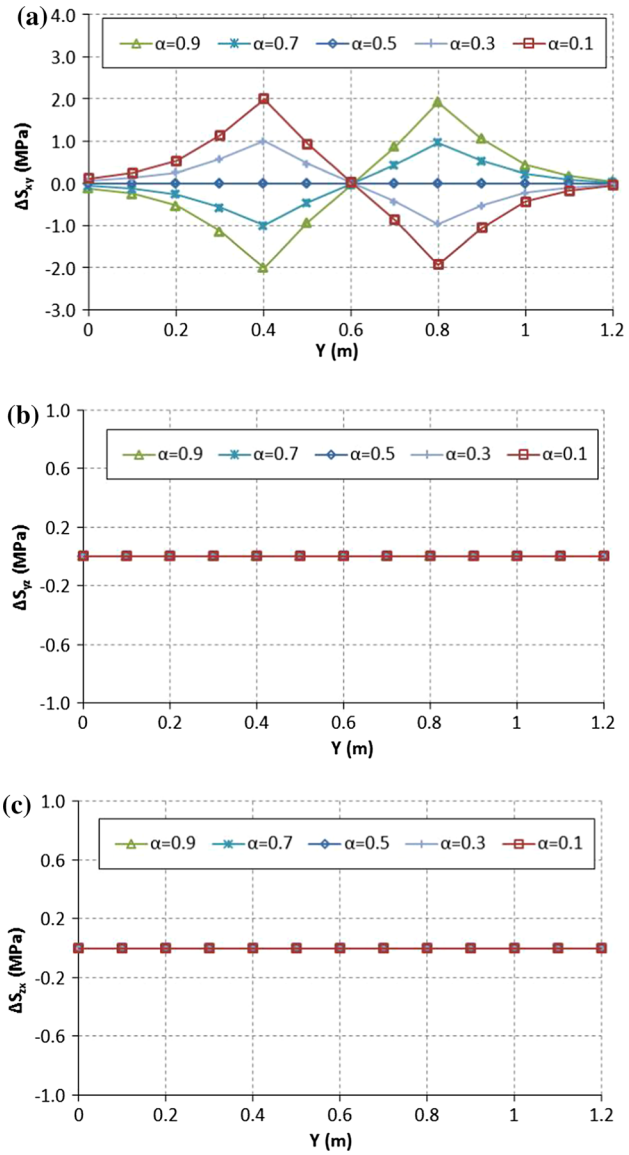

Fig. 23 Induced shear stresses along the line yy' (see Fig. 20) for cases using different Biot's effective stress coefficient between $y = 0.4$ m and $y = 0.8$ m: **a** ΔS_{xy}; **b** ΔS_{yz}; **c** ΔS_{zx}

situations, material properties, such as Young's modulus and permeability, could vary by a factor of two and more, especially when discontinuities (e.g., joints, natural fractures) exist. These sudden changes in material properties could be explicitly incorporated into the generated random fields.

Complex processes are involved in hydraulic stimulations, especially when the heterogeneous characteristics of geological formations are considered. For the sake of simplicity, some simplifying assumptions have been made, which may need to be improved when dealing with a real system, and are left for future research.

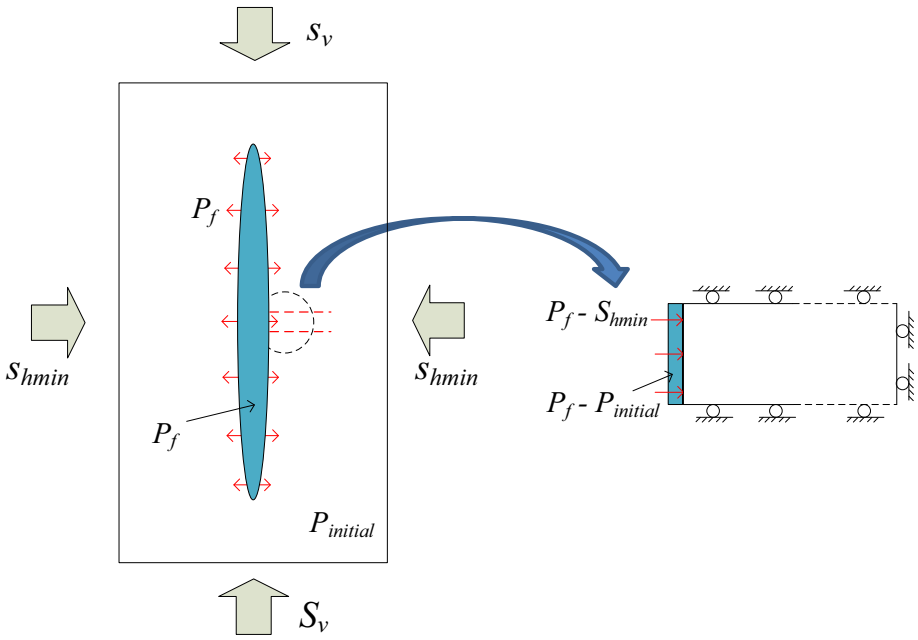

Fig. 24 1D fluid pressure loading condition on pressurized fracture surface

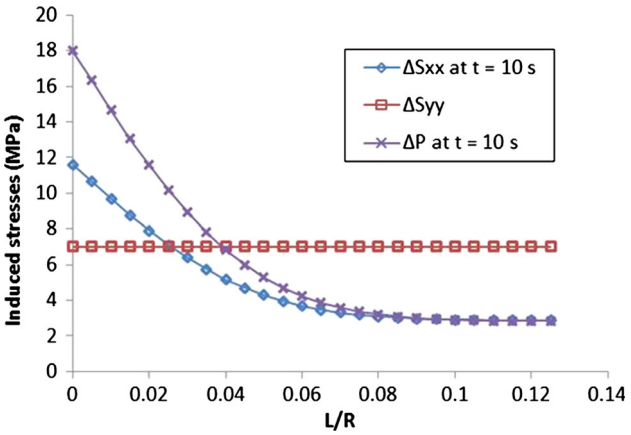

Fig. 25 Induced stresses and pore pressure for 1D fluid pressure loading. ΔS_{yy} equals to the applied net pressure during the process of fluid pressure diffusion

6 Conclusions

A fully coupled 3D poroelastic model based on FEM has been developed to analyze the stress and pore pressure distributions around a pressurized fracture in heterogeneous porous media. The heterogeneous distributions of Young's moduli and permeability are generated based on lognormal random distribution. Good agreement has been achieved between the analytical solutions and numerical results. Comparison of the pressurized fracture simulation results for a heterogeneous medium with those in a homogeneous one indicates that the normal stress component is almost the same in the two cases, but shear stresses in the heterogeneous media are significantly larger and vary as a function of time and thus are related with the diffusion of pore pressure. Our analyses show that shear stresses develop along the interfaces of materials with different properties (e.g., Young's modulus). Although normal stresses experience variations along the interfaces, their magnitudes are smaller than the generated shear stresses and much smaller than their initial values. Due to the spatial variation in material properties, shear stresses and nonuniform deformations are generated in a poroelastic rock surrounding a pressurized crack. The induced shear stresses in heterogeneous rock cause the initially horizontal principal stresses to rotate out of horizontal planes, which may potentially influence the propagation direction of subsequent fractures. As the pore pressure diffuses into the formation, the stress-reversal regions gradually disappear, and in areas where there has been stress rotation without a complete reversal, the rotation angles of the principal stresses decrease. The induced horizontal stress differential caused by the pressurization of the fracture is less than the original in situ horizontal stress differential in a region close to the fracture surface. As a result, the maximum horizontal stress remains larger than the minimum horizontal stress, and there will be no stress reversal in regions close to the fracture surface. This is in contrast to predictions based on an elastic formulation without consideration of the pore pressure diffusion effects on rock deformation.

References

Biot MA (1941) General theory of three-dimensional consolidation. J Appl Phys 12:155–164

Carter J, Booker J (1982) Elastic consolidation around a deep circular tunnel. Int J Solids Struct 18:1059–1074

Cheng AH-D (2016) Poroelasticity. Springer, Cham
Cheng AHD, Abousleiman Y, Roegiers JC (1993) Review of some poroelastic effects in rock mechanics. Int J Rock Mech Min Sci Geomech Abstr 30:1119–1126. doi:10.1016/0148-9062(93)90081-N
Detournay E, Cheng AH-D (1991) Plane strain analysis of a stationary hydraulic fracture in a poroelastic medium. Int J Solids Struct 27:1645–1662
Deutsch CV, Journel AG (1992) GSLIB, Geostatistical software library and user's guide. Oxford University Press, New York
Durlofsky LJ (1991) Numerical calculation of equivalent grid block permeability tensors for heterogeneous porous media. Water Resour Res 27:699–708
Fenton GA, Griffiths DV (2008) Risk assessment in geotechnical engineering. Wiley, Hoboken
Ge J, Ghassemi A (2008) Analysis of failure potential around a hydraulic fracture in jointed rock. Paper presented at the 42nd US rock mechanics symposium (USRMS), San Francisco, California
Ghassemi A, Roegiers JC (1996) A three-dimensional poroelastic hydraulic fracture simulator using the displacement discontinuity method. Paper presented at the proceedings of the 2nd North American rock mechanics symposium, Rotterdam
Ghassemi A, Zhang Q (2006) Porothermoelastic analysis of the response of a stationary crack using the displacement discontinuity method. J Eng Mech 132:26–33. doi:10.1061/(asce)0733-9399(2006)132:1(26)
Ghassemi A, Zhou X (2011) A three-dimensional thermo-poroelastic model for fracture response to injection/extraction in enhanced geothermal systems. Geothermics 40:39–49. doi:10.1016/j.geothermics.2010.12.001
Ghassemi A, Zhou XX, Rawal C (2013) A three-dimensional poroelastic analysis of rock failure around a hydraulic fracture. J Pet Sci Eng 108:118–127. doi:10.1016/j.petrol.2013.06.005
Gordeyev YN (1993) Growth of a crack produced by hydraulic fracture in a poroelastic medium. Int J Rock Mech Min Sci Geomech Abstr 30:233–238. doi:10.1016/0148-9062(93)92726-7
Guerillot DR, Lemouzy P, Ravenne C, Galli A (1990) 3D fluid flow behavior in heterogeneous porous media characterized by geostatistical method. Paper presented at the SPE Latin America petroleum engineering conference, Rio de Janeiro, Brazil, 14–19 Oct 1990
Kumar D, Ghassemi A (2015) Simulation of mixed-mode poroelastic fracture propagation for reservoir simulation. GRC Trans 39:937
Rawal C, Ghassemi A (2011) Poroelastic rock failure analysis around multiple hydraulic fractures using a BEM/FEM model. 26–29 June 2011
Rice JR, Cleary MP (1976) Some basic stress diffusion solutions for fluid-saturated elastic porous media with compressible constituents. Rev Geophys 14:227–241
Safari R, Ghassemi A (2015) 3D thermo-poroelastic analysis of fracture network deformation and induced micro-seismicity in enhanced geothermal systems. Geothermics 58:1–14. doi:10.1016/j.geothermics.2015.06.010
Sesetty V, Ghassemi A (2015) A numerical study of sequential and simultaneous hydraulic fracturing in single and multi-lateral horizontal wells. J Pet Sci Eng 132:65–76. doi:10.1016/j.petrol.2015.04.020
Sesetty V, Ghassemi A (2016) Numerical modeling of hydraulic fracture propagation from horizontal wells in anisotropic shale. Paper presented at the 50th US rock mechanics/geomechanics symposium, Houston, Texas, USA, 26–29 June
Smith IM, Griffiths DV (2004) Programming the finite element method, vol Book, Whole, 4th edn. Wiley, West Sussex
Sneddon IN (1946) The distribution of stress in the neighbourhood of a crack in an elastic solid. Proc R Soc Lon Ser A 187:229–260. doi:10.1098/rspa.1946.0077
Vandamme L, Detournay E, Cheng AHD (1989) A two-dimensional poroelastic displacement discontinuity method for hydraulic fracture simulation. Int J Numer Anal Methods Geomech 13:215–224. doi:10.1002/nag.1610130209
Wang X, Ghassemi A (2012) A 3D thermal–poroelastic model for naturally fractured geothermal reservoir stimulation. Paper presented at the 46th U.S. rock mechanics/geomechanics symposium, Chicago, Illinois, 24–27 June
Warpinski NR, Branagan PT (1989) Altered-stress fracturing. J Pet Technol 41:990–997. doi:10.2118/17533-pa
Warren JE, Price HS (1961) Flow in heterogeneous porous media. Soc Pet Eng J. doi:10.2118/1579-g
Zhou X, Ghassemi A (2011) Three-dimensional poroelastic analysis of a pressurized natural fracture. Int J Rock Mech Min Sci 48:527–534. doi:10.1016/j.ijrmms.2011.02.002